Journal of Applied Physics

# Effects of polycrystalline birefringent grains on the morphology dependent resonance modes of a spherical resonator

Cite as: J. Appl. Phys. **126**, 053102 (2019); https://doi.org/10.1063/1.5094333
Submitted: 28 February 2019 . Accepted: 15 July 2019 . Published Online: 05 August 2019

Imon Kalyan, and C. V. Krishnamurthy

Journal of Applied Physics ARTICLE scitation.org/journal/jap

# Effects of polycrystalline birefringent grains on the morphology dependent resonance modes of a spherical resonator

Cite as: J. Appl. Phys. **126**, 053102 (2019); doi: 10.1063/1.5094333
Submitted: 28 February 2019 · Accepted: 15 July 2019 ·
Published Online: 5 August 2019



Imon Kalyan[a] and C. V. Krishnamurthy

## AFFILIATIONS

Department of Physics, Indian Institute of Technology Madras, Chennai, Tamilnadu 600036, India

[a]**Email:**kalyanimon1@gmail.com

## ABSTRACT

Morphology dependent resonance (MDR) modes in a dielectric sphere are highly sensitive to its shape, size, and refractive index (RI). Many dielectric materials with potential applications are birefringent in nature. Synthesis techniques of resonators of such materials may lead to polycrystalline morphologies. Due to its fascinating applications, titanium dioxide ($TiO_2$) has attracted attention as a morphology dependent resonator. However, its high RI is accompanied by high birefringence. The effect of the grains on resonance modes is the interest of this study. Polycrystalline $TiO_2$ microspheres with different grain distributions are synthesized by annealing at 500 °C and 700 °C. MDR modes in the photoluminescence spectrum of single spheres are found to exhibit mode splitting and mode shifting with respect to MDR modes of an equivalent isotropic sphere. The MDR spectral features of the near-perfect spheres have been investigated for the perturbative effects due to (a) nonsphericity and surface roughness and (b) inhomogeneity in RI arising from polycrystallinity and annealing conditions. Mode splits are demonstrated to arise from the perturbative effects of the larger grains through explicit computations using discrete dipole approximation for a Voronoi tessellated cell structure representing a polycrystalline sphere. Mode shifts are demonstrated to arise from radial inhomogeneity of the refractive index using the Aden-Kerker theory on spheres with core-shell morphology. The effects of surface roughness are not found to be significant. The present work extends the scope of model-assisted investigations in understanding morphology dependent resonators and indicates the possibility of designing resonators with prescribed refractive index features.



## I. INTRODUCTION

Light incident on a microsphere of radius greater than its wavelength (WL) can be trapped due to the total internal reflection at its surface. This phenomenon results in morphology dependent resonance (MDR) modes in its spectrum.[1] These resonance modes are also known in the literature as whispering gallery modes (WGMs).[1,2] Spectral positions of such resonances are dependent on the morphology and refractive index (RI) of the constituting material and the surrounding medium. These modes have been important for their various potential applications such as sensing, filtering, microlasing, nonlinear photonics, etc.[3–6] These resonance modes can be excited by applying extrinsic frequencies and intrinsic frequencies. Intrinsic frequencies can be generated by coupling the particles with fluorescent dye[6,7] or nanodots[8,9] or by exciting the photoluminescence (PL) of the intrinsic material.[10–12] Compound semiconductors, such as ZnO,[10,11] $TiO_2$,[12–16] SiN,[17] GaN,[18] etc., have been studied largely as morphology dependent resonators due to their fascinating optical properties. Most of these materials are birefringent in nature. Many routes of synthetization, such as pulsed laser deposition,[10] chemical vapor deposition,[17] hydrothermal,[11] sol-gel,[12–14] etc., have been used to produce resonators with potential applications. Such routes are useful in modifying the optical properties of the materials at the molecular or elementary stage of synthesis. Crystallization of particles made of such birefringent materials can lead to structures with polycrystalline morphologies. While crystallization can improve the optical properties and the stability of the material, the resonance characteristics can get perturbed due to their birefringent and polycrystalline morphology.

$TiO_2$ has attracted attention due to its suitable chemical, optical, and electronic properties. It has been suitable as a morphology dependent resonator due to various properties like high scattering and low absorption in the visible and infrared spectrum,[19] low

thermal expansion coefficient, CMOS compatibility for silicon photonic devices,[13] biocompatibility, chemically stable nature,[14] etc. $TiO_2$ is popularly known for its photocatalytic activity. MDR in $TiO_2$ spheres can enhance the photocatalytic activity[12,16] making it more efficient in solar cell applications.[20]

Most of the chemical routes of synthesis of $TiO_2$ resonators result in the amorphous phase.[13,15] The amorphous phase of $TiO_2$ is unstable and converts to crystalline phases on thermal treatments above 350 °C.[12,13,21] The thermal treatment above 500 °C can result in the growth of the rutile phase of $TiO_2$.[13,21] The phase transition temperature is found to be dependent on the method of preparation.[13,21–24]

$TiO_2$ in its crystalline form has a higher refractive index as compared to that in its amorphous form and also has high birefringence.[13,19,25,26] Refractive index and birefringence are greater in the rutile phase as compared to those in the anatase phase.[19] In most of the synthesis routes for the rutile phase, high temperature thermal treatments are used, resulting in larger crystal grain sizes.[22,24] However, since larger grain sizes lead to higher anisotropy, rutile polycrystals are not preferred as spherical resonators in the optical region. Optical resonators made of $TiO_2$ materials are mostly either amorphous[13,15,27] or anatase polycrystals obtained by treating at lower temperatures.[12,28] Amorphous $TiO_2$ is thermally unstable. Exposure to high temperature, high power laser beam, or electron beam can result in the crystallization of amorphous $TiO_2$.[21,29] Though anatase $TiO_2$ also has a tendency to change its phase to rutile, when its grains are bigger, it has a better thermal stability against phase transition.[24] Resonators made of anatase $TiO_2$ polycrystals with bigger grain sizes would be suitable for thermal sensing and other practical applications due to their stability against phase transition. MDR modes have been studied in single crystalline[26,30] and polycrystalline $TiO_2$ resonators.[12,16] However, the effects of the sizes and distribution of the birefringent grains of a resonator on their MDR modes have not been explored systematically to the best of our knowledge.

In the present work, MDR modes of anatase $TiO_2$ microspheres with larger grain sizes are studied experimentally and through simulations. Microspheres with different grain sizes are obtained by annealing the amorphous spheres at different temperatures. Annealing leads to internal changes involving grain growth and realignments. From x-ray, Raman spectra, and images of the surfaces obtained using scanning electron microscopy (SEM), the medium has been identified to be made up of anatase crystallites. Since the initial samples are amorphous and the annealing conditions are on a gross scale, the final state, while corresponding to the anatase phase, may not have a unique grain size distribution in terms of sizes and orientations. MDR spectra appear to provide some insight into the details of the internal structure as the grain sizes and orientations influence the optical response. An equivalent isotropic sphere (EIS) having the same size as the experimental sphere is simulated using a recently developed procedure by Kalyan and Krishnamurthy[16] Systematic differences between the observed MDR spectra and the MDR spectra of an equivalent isotropic sphere are identified and investigated. The trends of these observed differences could be explained by two simple models: (a) polycrystalline morphology with randomly oriented birefringent grains and (b) radially inhomogeneous RI distribution.

Section II describes the experimental aspects related to the preparation and characterization of the samples under investigation. Section III presents the experimental MDR modes and a detailed comparison between MDR spectra computed for the EIS and the experimental MDR spectra. The observed deviations are analyzed in Sec. IV in terms of perturbation caused by (A) surface roughness and nonsphericity and (B) inhomogeneous distribution of RI due to crystallization. The conclusion drawn from the present study indicates that the MDR spectra can be used as a sensitive tool to probe the internal structure.

## II. EXPERIMENTAL INVESTIGATIONS

### A. Sample preparation

Titanium dioxide microspheres are obtained by solvothermal treatment of titanium isopropoxide (TTIP) in ethanol following the method described by He *et al.*[31] 1.6 ml of TTIP (97%) is dissolved in 38 ml ethanol followed by the addition of 0.4 ml formic acid to obtain a transparent solution. This solution is then transferred to a Teflon lined autoclave of 50 ml capacity to fill 80% of its volume. The autoclave is then heated at 150 °C for 1 h. After this heat treatment, sediment particles are collected by centrifugation and cleaned with ethanol several times. $TiO_2$ microspheres 1.5 $\mu$m diameter on average is obtained. These particles are dispersed in ethanol and drop-casted on a silicon substrate. These drop-casted particles are dried at 150 °C for 3 h followed by annealing at 500 °C and 700 °C for a duration of 2 h to obtain spheres with different crystalline morphologies. The samples annealed at 500 °C and 700 °C are designated as S-500 and S-700, respectively.

According to He *et al.*,[31] TTIP in ethanol undergoes an alcoholysis reaction to produce a modified titanium precursor at room temperature. During the solvothermal process, the $TiO_2$ gel is produced, which gets condensed with a high degree of cross linking. As the solvothermal reaction precedes, these gel particles grow in size and finally take a spherical shape within an hour. The solvothermal treatment is carried out for 1 h to produce spherical $TiO_2$ microparticles made of amorphous nanoparticles.[31] When undergone annealing, the constituent amorphous nanoparticles get crystallized to the anatase phase. The sizes of the grains increase as annealing temperature is increased.[22] Size and distribution of the grains depend on the annealing temperature.[32]

### B. Sample characterization

The phase of the synthesized particles is determined with Raman spectrometry and X-ray diffractometry using a Horiba Jobin Vyon HR 800 UV Raman spectrometer and a Rigaku D/Max-2500 x-ray diffractometer (Cu-K$\alpha$), respectively. Images of the single spheres and their surfaces were collected with high resolution SEM (Inspect F50 FESEM, Hitachi S4800 HR-SEM).

The Raman spectra of a single spherical particle excited by an argon ion laser (488 nm) for each S-500 and S-700 are shown in Figs. 1(a) and 1(b), respectively. The peaks at 144.54 ($E_g$), 197.18 ($E_g$), 397.78 ($B_{1g}$), 521.4 ($A_{1g} + B_{1g}$), and 640.3 ($E_g$) corresponding to the Raman spectra of S-500 and those at 143.31 ($E_g$), 195.86 ($E_g$), 395.94 ($B_{1g}$), 520.29 ($A_{1g} + B_{1g}$), and 640.91($E_g$) corresponding to the Raman spectra of S-700 confirm their phases

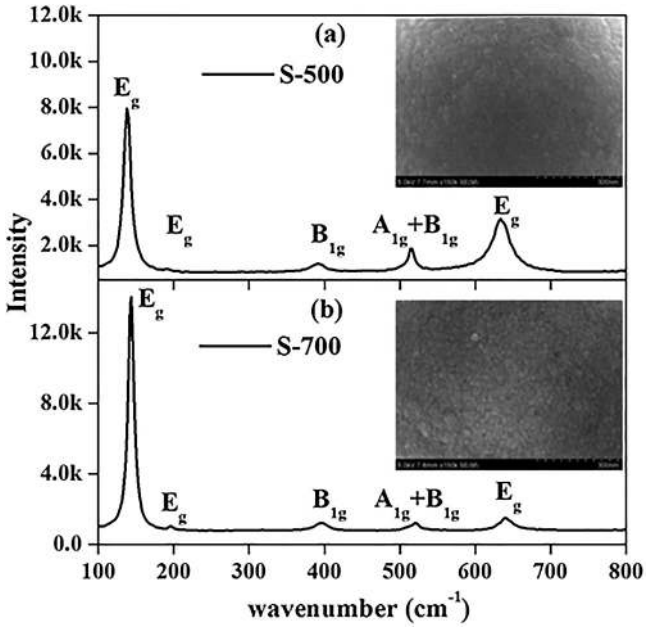


**FIG. 1.** Raman spectrum of (a) S-500 and (b) S-700. The insets in (a) and (b) are the high resolution SEM image (without gold coating) of the surfaces of the spheres corresponding to S-500 and S-700, respectively.

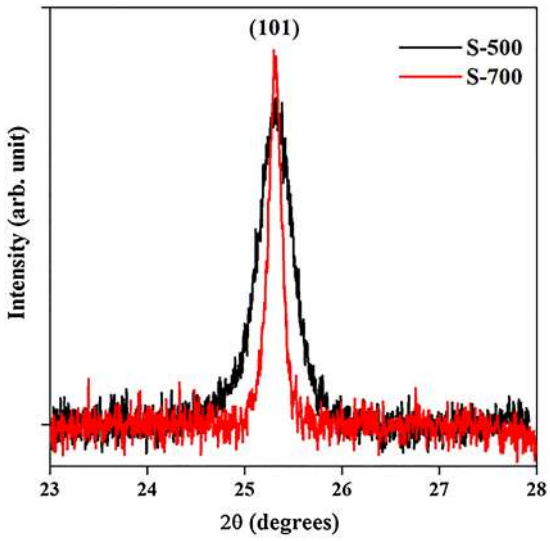


**FIG. 2.** (101) peak in the XRD of S-500 (black) and S-700 (red).

to be anatase $TiO_2$.[22] The full width at half maximum (FWHM) of the most significant (the first) Raman peak, 11.61 $cm^{-1}$ and 9.29 $cm^{-1}$ for S-500 and S-700, respectively, indicates the presence of bigger crystal grains in S-700 as compared to S-500. The SEM images of the surfaces of the spheres corresponding to S-500 and S-700, shown in the insets of Figs. 1(a) and 1(b) respectively, also indicate the presence of comparatively bigger grain sizes in S-700 as compared to S-500. The XRD pattern obtained from the drop-casted films of the microspheres after heat treatments also indicates their phase to be anatase. The (101) peak of XRD data (Fig. 2) of both the samples being well above the noise level is used to estimate the average crystalline size. The decrease in the FWHM of (101) peak for S-700 as compared to that of S-500 indicates that the average grain size in S-700 is greater than that in S-500. Average crystal sizes of the particles, calculated from the (101) peak of XRD data using the Scherrer formula, are 21.3 nm and 54.6 nm for S-500 and S-700, respectively.

Photoluminescence (PL) of an isolated single microsphere is obtained by a micro-Raman spectrometer with an excitation energy of 2.54 eV. The PL spectrum is recorded in a range of WL much away from the Raman lines of anatase $TiO_2$. The photoluminescence observed in the visible spectrum may be attributed to the interband transitions from the defect states due to oxygen vacancies as the excitation energy is much below the bandgap (3.2 eV) of pure anatase $TiO_2$.[12,23,33] MDR modes are observed on the top of the wide PL spectrum of a single sphere of each S-500 and S-700. The observed MDR modes and their identification are briefly discussed in Sec. III.

## III. ANALYSIS OF EXPERIMENTAL MDR MODES

### A. Analysis based on the effective isotropic medium approach

MDR modes observed in the PL spectrum of a sphere are analogous to the scattering efficiency ($Q_{sca}$) spectrum of that sphere.[1] From a ray optics point of view, MDR modes occur in a sphere of radius $a$ with a medium of RI $n$ when the WL of the incident light ($\lambda$) satisfies Eq. (1),

$$\frac{2\pi an}{\lambda} = l, \tag{1}$$

where $l$ is an integer. However, Eq. (1) is more convincing when $l \gg 1$. In general, light scattering by an isotropic and homogeneous spherical body can be described by the Mie–Debye theory.[1,34] Mode conditions in terms of size parameters ($x = 2\pi a/\lambda$) are given by Eqs. (2a) and (2b) for transverse electric (TE) and transverse magnetic (TM) modes, respectively,

$$\frac{[xh_l^1(x)]'}{h_l^1(x)} = \frac{[nxj_l(nx)]'}{j_l(nx)}, \tag{2a}$$

$$\frac{n^2[xh_l^1(x)]'}{h_l^1(x)} = \frac{[nxj_l(nx)]'}{j_l(nx)}, \tag{2b}$$

where $h_l = j_l + iy_l$ is the spherical Hankel function and $j_l$ and $y_l$ are the spherical Bessel and Neumann functions, respectively. The primed terms are their derivatives with respect to the variables inside the corresponding parentheses.

The MDR modes are represented by four parameters: polarization (TE/TM), angular momentum mode number ($l$), radial mode number ($\rho$), and azimuthal mode number ($m$) and are labeled as $TE_{l,\rho}$ (or $TM_{l,\rho}$). The angular momentum mode number

$l$ can be obtained from Eq. (2). For a particular value of $l$, Eq. (2) can have several solutions; each solution is assigned a different value of $\rho$. The solution with the lowest energy (longest wavelength) are known as fundamental modes[2] and assigned the value of $\rho = 1$. The number of intensity maxima along the great perimeter of the sphere and along the radial direction of the sphere is indicated by $l$ and $\rho$, respectively. Modes with higher values of $l$ and lower values of $\rho$ tend to take a Lorentzian profile with a very high quality ($Q$) factor. Equations (2a) and (2b) are independent of azimuthal mode number $m$ and so the spectral positions of MDR modes in an isotropic homogeneous sphere are independent of $m$.[1,2] In a perfect spherical resonator, for a particular value of $l$, the value of $m$ can lie in the range of $-l$ to $+l$ with $2l + 1$ fold degeneracy. However, the spatial pattern of field distribution is dependent on the value of $m$. The spectral degeneracy can be lifted due to the effect of spatial perturbation caused by various factors like deformation in the spherical shape,[35,36] the presence of inhomogeneous inclusions,[37] birefringence of the constituting material,[2,38] etc. Le Floch *et al.*[2] have discussed the dependence of the field distribution and lifting of degeneracy related to $m$ in detail for MDR modes excited at MHz frequency. This discussion is also applicable at optical frequencies of interest in the present study. The lifting of degeneracy can result in broadening or deformation of the Lorentzian profile associated with a mode.

MDR modes observed in the PL spectra corresponding to S-500 and S-700 are presented in Figs. 3(b) and 4(b), respectively. The Lorentzian shape of some of the MDR modes in the observed PL spectra are deformed (mostly in S-700) because of perturbations present in the sphere. To investigate the perturbations involved in the deformation of the MDR modes, the sphere is compared to an equivalent isotropic sphere with the same diameter and an effective refractive index (ERI) deduced by the method recently proposed by Kalyan and Krishnamurthy.[16] In this method, the radius and wavelength of the incident light are obtained from the SEM image and the MDR spectrum, respectively. The ERI is deduced using Eq. (3) for TE modes,[39] when $x$ is in the domain $1 \ll x < l$,

$$n y_l(x) j_l'(nx) - y_l'(x) j_l(nx) = 0. \tag{3}$$

By minimizing the differences ($\Delta\lambda_{l,\rho}$) between the mode positions calculated using the extracted ERI and those obtained from the experiment, the mode positions are predicted through $l$-based trials, in the least square sense. While $\rho = 1$ modes were used in the earlier work, RI has been extracted using $\rho = 2$ modes in the present study as they are observed to be the least perturbed in both S-500 and S-700. However, for the correct assignment of $l$, the spectral mode positions of $\rho = 1$ modes of the experimental spectrum are also observed to be the ones close to the calculated mode positions. The details of the mode identification and RI extraction method can be found in the study by Kalyan and Krishnamurthy.[16]

The scattering efficiency spectra of EIS corresponding to S-500 and S-700 calculated using MiePlot[40] after correction of refractive index for S-500 and S-700 are shown in Figs. 3(a) and 4(a), respectively. The dispersive RI extracted using $\rho = 2$ modes are then fitted with the Sellmeier dispersion relation for S-500 (in black) and S-700 (in blue) are presented in Fig. 5. The weighted average values of ordinary and extraordinary RIs of bulk anatase $TiO_2$[19] (in gray) are also shown in Fig. 5. While the RI of both S-500 and S-700 are found to be significantly lower than that of bulk anatase, the RI of S-700 is seen to be systematically higher than that of S-500.

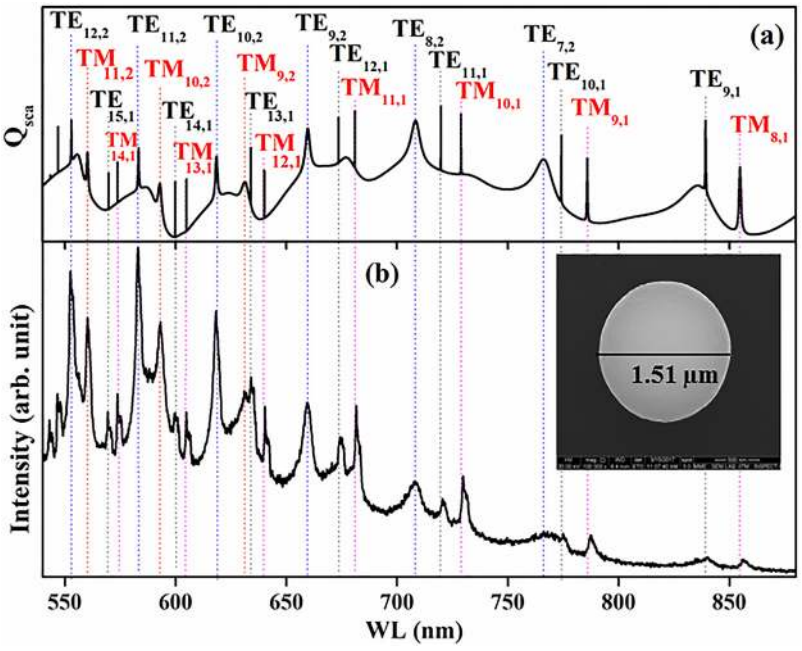


**FIG. 3.** For S-500: (a) simulated scattering efficiency for EIS corresponding to (b) the PL spectrum. The inset is the SEM image of the corresponding sphere. The diameter of the sphere is 1.51 $\mu$m.

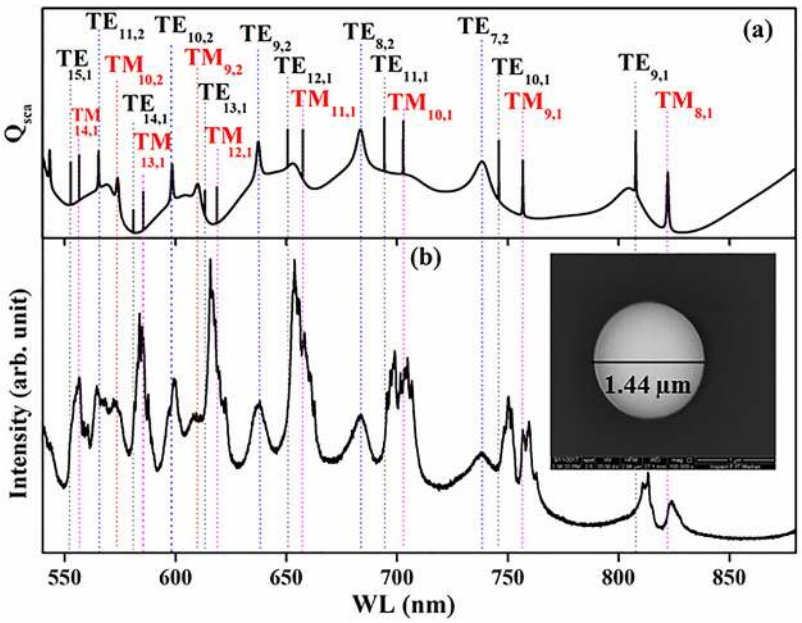


**FIG. 4.** For S-700: (a) simulated scattering efficiency for EIS corresponding to (b) the PL spectrum. The inset is the SEM image of the corresponding sphere. The diameter of the sphere is 1.44 $\mu$m.

### B. Deviations with respect to the MDR spectra of EIS

The observed spectra differ from the computed spectra of its EIS in two ways. The observed resonance peaks show breakups and small relative shifts in spectral positions with respect to those computed for its EIS. The extent of splits and shifts is found to depend on polarizations, $l$ and $\rho$, which in turn depend on the particle's size and RI.

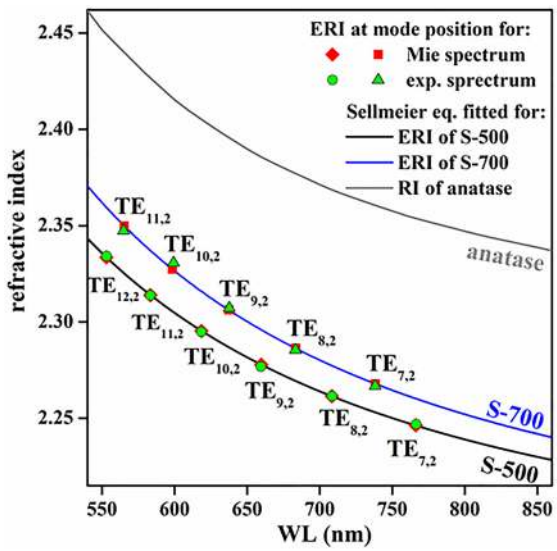


**FIG. 5.** ERI extracted from $\rho = 2$ resonant mode positions for S-500 (black line) and S-700 (blue line) as a function of wavelength are shown. The spectral positions and corresponding estimated RI from the experiment for S-500 and S-700 are depicted by (green filled) circles and triangles, respectively, and that from simulated scattering efficiency spectra are depicted by (red filled) diamonds and squares, respectively. The RI for bulk anatase (gray line) is included for reference.

Perturbed modes can be observed in both the emission spectra of S-500 and S-700. The modes with lower values of $l$ and higher values of $\rho$ are the least affected and retain their Lorentzian shape. However, as $l$ increases, it becomes increasingly difficult to fit a single Lorentzian shape to the mode structure. For $\rho = 1$ modes, convolution of multiple Lorentzians is necessitated for the fit revealing splits. Figure 6 illustrates the effect of perturbation in TM modes with $l = 7$, 8, and 9 of the MDR spectra of S-700. It can be observed that $TM_{7,1}$ in Fig. 6(a) can be fitted well with a single Lorentzian. $TM_{8,1}$ in Fig. 6(b) shows that a fit to a single Lorentzian is poor. Though splitting cannot be seen directly in $TM_{8,1}$, it can be deconvolved into two peaks. $TM_{9,1}$ can be observed to be a convolution of three Lorentzians, and splits can be seen explicitly in Fig. 6(c).

In S-500, all modes are distinguishable. As modes with a higher value of $l$ are found to be more perturbed, only those modes with the highest values of $l$ occurring at the shortest wavelength under consideration are shown in Fig. 7(a). It can be observed that in the spectrum of S-500, on the other hand, the mode with even the highest value of $l$ is distinguishable and a Lorentzian can be fitted to obtain its mode position. As shown in Fig. 7(b), the $TE_{16,1}$ mode in S-500 is observed to have three major points of maxima at 543.0, 544.1, and 544.6 nm. As the $TE_{16,1}$ mode remains distinct, despite its broken structure, a Lorentzian profile is fitted as shown in Fig. 7(b) by a dashed line. The fitted Lorentzian may be regarded as a representative of the $TE_{16,1}$ mode of an equivalent isotropic sphere having the size as observed in SEM (radius 1.51 $\mu$m). $\rho = 2$ modes also show distortion from Lorentzian shape for $l > 10$, which can be observed in Fig. 7(a); however, prominent splits are not observed.

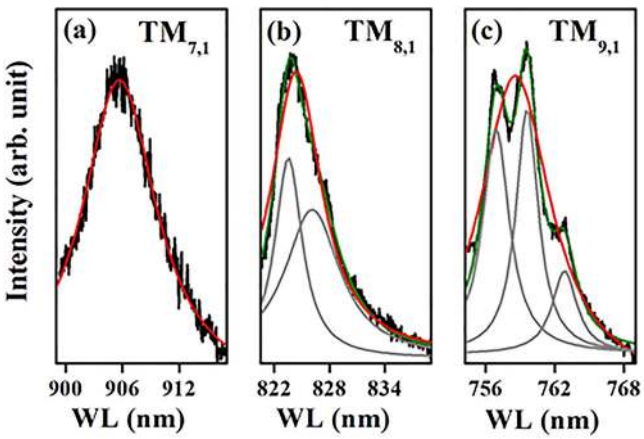


**FIG. 6.** (a) $TM_{7,1}$, (b) $TM_{8,1}$, and (c) $TM_{9,1}$ modes of S-700 indicating Lorentzian, distorted Lorentzian, and split spectral features, respectively, of an MDR mode. Black colored curve indicates recorded data, and the red colored curve indicates a fit to a single Lorentzian. The gray colored curves correspond to the multiple Lorentzians used to convolve the recorded data in (b) and (c). The convolved resultant is indicated by the green color.

In the MDR spectrum of S-700, all observed modes are not distinguishable. Figure 8(a) shows that the $\rho = 1$ modes beyond $TE_{11,1}$ and $TM_{10,1}$ cannot be distinguished as they merge with the neighboring modes. Fitting of Lorentzian for the estimation of mode positions of $TE_{11,1}$ and $TM_{10,1}$ modes is shown in Fig. 8(b). In the range of 690–714 nm, seven split peaks are observed in the experimental spectrum, which can be deconvoluted to two

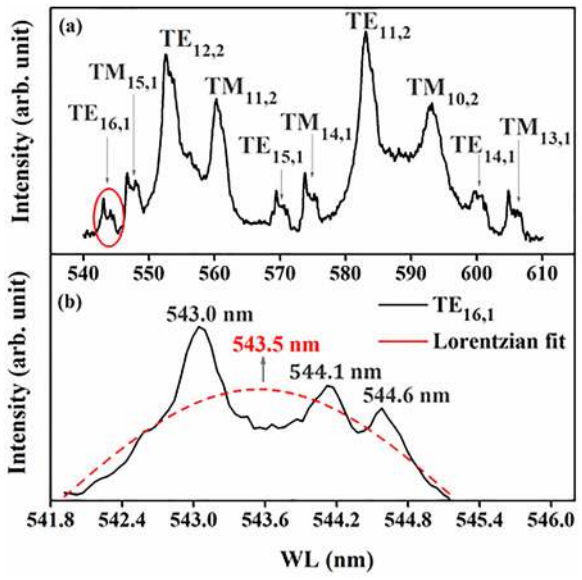


**FIG. 7.** (a) PL spectrum in a small range for S-500. (b) Lorentzian fitted (dashed line) to the $TE_{16,1}$ mode highlighted in (a).

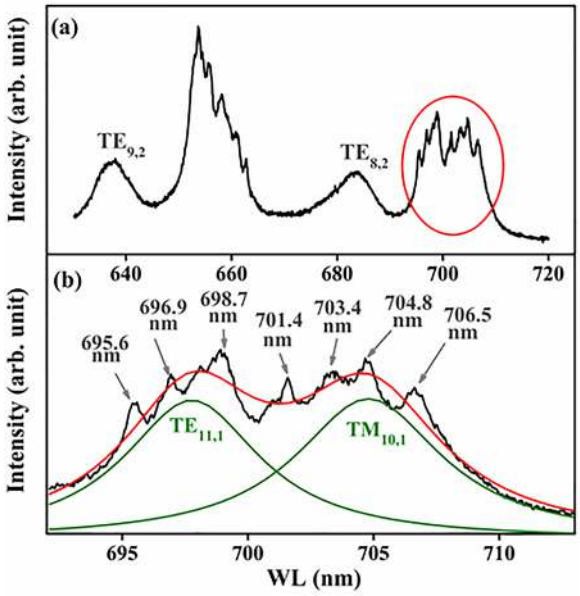


**FIG. 8.** (a) PL spectrum in a small range for S-700. (b) Lorentzian fitted to $TE_{11,1}$ and $TM_{10,1}$ modes by deconvolution.

Lorentzians centered at 697.8 and 704.8 nm, respectively, to represent the $TE_{11,1}$ and $TM_{10,1}$ modes of an equivalent isotropic sphere having the size as observed in SEM (radius 1.44 $\mu$m). However, $TE_{12,1}$ and $TM_{11,1}$ modes are observed to be merged into one another, and it is very difficult to distinguish their mode positions by Lorentzian fitting. The $\rho = 2$ modes start showing up distortion as $l$ increases. The trends in the observed mode splits are summarized in Table I. The spectral positions of the experimental MDR modes and of the modes corresponding to the EIS estimated in the least square sense (min of $\langle(\Delta\lambda_{l,\rho})^2\rangle$) are provided in Table II for S-500 and in Table III for S-700 in Appendix A.

The experimental $\rho = 2$ mode positions appear close to the EIS spectral mode positions, unlike the experimental $\rho = 1$ modes that seem slightly red shifted with respect to those of the EIS spectral mode positions in S-500. This shift is more prominent in the case of S-700. The mode positions of the spectra of S-700 obtained from experiment and those of its best estimated EIS are presented in Fig. 9. In the spectrum of S-700, modes with higher values of $l$ are too close to be distinguished from each other. TE modes with $l > 12$ appear to merge with the nearest TM modes with $l > 11$ and are indistinguishable from each other and hence not presented.

The synthesized spherical particles consist of amorphous nanoparticles[31] before crystallization. As the RI of amorphous $TiO_2$ is known to be lower than that of its crystalline phase,[13,25] the as-synthesized spheres have lowered ERI values. On crystallization, although ERI of the sphere increases, it is observed to be still less than that of the weighted average bulk RI.[19] The lowered RI appears to be due to the porosity that still exists due to the voids between the grains that can be seen in the high resolution SEM images of the surfaces of S-500 and S-700 in the inset of Figs. 1(a) and 1(b), respectively.

**TABLE I.** Trends in the splitting of experimental MDR modes.

| | S-500 | S-700 |
|---|---|---|
| $\rho = 1$ | (a) All modes are either distorted or split Lorentzians<br>(b) Splitting is over a narrow wavelength range<br>(c) Peaks are distinguishable and merging of peaks with different $l$ and polarization are not observed | (a) All modes are either distorted of split Lorentzians<br>(b) Splitting is over a broader wavelength range<br>(c) Modes with higher values of $l$ are too close to be distinguished from each other. TE modes with $l > 11$ appear to merge with the nearest TM modes with $l > 10$ and are indistinguishable from each other |
| $\rho = 2$ | (d) Splitting not observed<br>(e) Slight distortion appears for modes with $l > 10$<br>(f) All modes are well distinguishable | (d) Splitting not observed<br>(e) Higher modes ($l > 9$) are distorted to a greater extent<br>(f) Modes with $l > 10$ are not well distinguishable |

When the annealing temperature increases, the crystal grains grow in size and the porosity in them is reduced resulting in a slight increase in RI. The relative increase in the ERI for S-700 over that for S-500 may be attributed to the reduction of void in the former. Furthermore, due to the annealing of the spheres at a higher temperature, the average size of the crystalline grains is bigger in S-700 compared to S-500 as confirmed by the reduction of FWHM of the XRD peak corresponding to (101) planes in S-700 compared to S-500 (see Fig. 2). There is a possibility of grain growth within the sphere at higher annealing temperatures. As $TiO_2$ is a birefringent material, bigger grains lead to local changes of RI within the sphere. These local changes in RI are considered to be the source for the perturbation of MDR modes, which is described in greater detail in Sec. IV.

## IV. PERTURBATION IN MDR MODES

The splitting and shifting of the MDR modes can be explained with the perturbation theory. According to the first order perturbation theory, the change in RI in a small volume $V_p$, inside or close to the sphere of volume $V$, changes the angular frequency ($\omega_{\mu 0}$) of the unperturbed MDR mode as given in Eq. (4),[1]

$$\delta\omega_\mu = -\frac{\omega_{\mu 0}}{2}\frac{\int_{V_p}\delta\varepsilon\mathbf{E}_\mu^*\cdot\mathbf{E}_\mu dV}{\int_V \varepsilon_r\mathbf{E}_\mu^*\cdot\mathbf{E}_\mu dV}, \tag{4}$$

where $\mathbf{E}_\mu$ is the electric field corresponding to the $\mu$th MDR mode. $\mu$ represents an MDR mode characterized by $l$, $\rho$, $m$, and polarization.

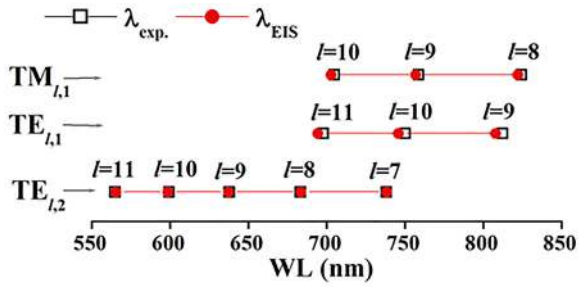


**FIG. 9.** Mode positions of S-700 for experimental spectrum (open squares) and as predicted for the spectrum of the EIS (filled red circle).

$\varepsilon_r = n^2$ and $\delta\varepsilon = n_p^2 - n^2$ are the relative permittivity of the unperturbed sphere and change in permittivity due to the perturbed RI, $n_p$, respectively. The radial distribution of $\mathbf{E}_\mu$ is dependent on $l$, $\rho$, and polarization characteristics of the mode. $\mathbf{E}_\mu$ corresponding to a large $l$ and a small $\rho$ has a higher value and a narrower distribution and hence contributes more to the perturbation effects.

For an isotropic homogeneous sphere, $\omega_{\mu 0}$ is independent of $m$. However, the angular distribution of $\mathbf{E}_\mu$ inside the sphere is different for different values of $m$. Perturbation can occur anywhere within a sphere, lifting the degeneracy with respect to $m$. This results in unequal amounts of shifting of mode frequencies for different values of $m$. When this shift is reasonably small, the affected modes appear to get broadened and hence its $Q$-factor gets reduced. When shifting of the modes is high enough to be resolved, a mode split appears.

The lifting of degeneracy of the MDR modes observed in the experimental spectrum can, in general, be attributed to the broken spherical symmetry occurring from structural deviations from a perfect sphere in terms of surface roughness and nonsphericity as well as from inhomogeneous RI distribution of the internal medium.

### A. Perturbation due to surface roughness and nonsphericity

SEM images of the surfaces of the spheres (insets in Fig. 1) indicate that the spheres are locally smooth. Though the grains at the surface of S-700 are comparatively larger than S-500, they are much smaller than the wavelength of the spectra of interest to result in accountable perturbation.

Though the analyzed spheres have good surface quality, they may not be having perfect sphericity. The simplest well studied perturbed spherical shape is that of an ellipsoid. The shift of mode position due to an ellipsoid with eccentricity $e$ is given by[35,36]

$$\frac{\delta\lambda}{\lambda_o} = \frac{e}{6}\left[1 - \frac{3m^2}{l(l+1)}\right]. \tag{5}$$

The eccentricity $e$ is defined by $e = \frac{a_p - a_e}{a_{eq}}$, with $a_p$ , $a_e$, and $a_{eq}$ denoting the polar, equatorial, and equivalent radii of the ellipsoid, respectively. Equation (5) indicates that the shift in the MDR modes is proportional to eccentricity and depends on the value of $m$. $\delta\lambda$ can be +ve or −ve with respect to $\lambda_0$ depending on the value of $m$.

The broadening of an MDR due to lifting of degeneracy estimated from the extreme values of $m$, i.e., $m = 0$ and $m = l$, is given by

$$|\delta\lambda_{m=l} - \delta\lambda_{m=0}| = \frac{e\lambda_0 l}{2(l+1)}. \quad (6)$$

When the eccentricity is small, modes corresponding to different $m$ values suffer little shift resulting in overlapping with each other causing broadening of the original mode. However, when eccentricity is large, modes corresponding to different $m$ values would separate from each other considerably, leading to a split of the original mode.

To determine the asphericity related to the spheres, SEM images were processed to obtain two colored images using ImageJ software as shown in Fig. 10. An ellipse was fitted to each of the processed images of the spheres using Matlab image processing function "regionprops." The difference between the major and minor axis was found to be 17 pixels (~41 nm) and 1 pixel (~3 nm) for S-500 and S-700, respectively, with ellipse orientations of 84° and 10°. This would indicate that eccentricity of S-500 is more than S-700. Consequently, MDR modes of S-500 are expected to be more perturbed. However, this is not borne out by the experimental observation. The width calculated using the value of $e$ is found to be of the order of FWHM of the experimental modes in S-500. However, the $l$ dependence shown by Eq. (6) is not borne out by the observed spectra. It appears that there may be other contributions to the observed trends in addition to nonsphericity. Widths of the modes calculated using the $e$ for S-700 are found to be much lesser than the FWHM of the experimental modes. The $l$ dependency of the FWHM is also not following Eq. (6). As $e$ is higher in S-500, the FWHM of S-500 is expected to be greater as compared to S-700. This is not observed in the recorded spectrum. Effects of polycrystallinity may dominate the spectra of S-700 more than that of S-500. This conclusion is also supported by the presence of larger grain sizes in S-700.

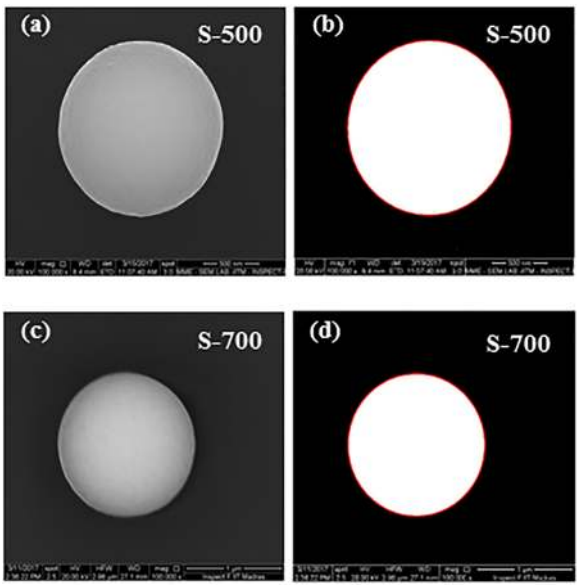


**FIG. 10.** SEM images of the spheres corresponding to S-500 and S-700 are shown in (a) and (c), respectively. The two color conversion and the corresponding fitted ellipse (in red color) using the "regionprops" function of Matlab are shown in (b) and (d) for S-500 and S-700, respectively.

To estimate the extent of nonsphericity, the diameter of the sphere is measured at 16 regular angular intervals. A spread is observed in the measurement. The mean and standard deviation of these measurements are 1507 nm and 15 nm for S-500 and 1439 nm and 5.8 nm for S-700, respectively. These values also indicate that the extent of nonsphericity is expected to be more in S-500 as compared to S-700. Again, the experimental results do not support this expectation. Thus, the effect of perturbation observed in S-700 cannot be explained in terms of structural deviation from a perfect sphere alone.

With the annealing temperature being below the melting or oxidation temperatures of the silicon substrate, reflow is also unlikely to take place. Particles are attached to the surface of the Si substrate only by van der Waal's forces. When annealed, the spheres get crystallized and smaller grains fuse to produce bigger ones. Only isolated spheres are considered for the study. So the fusion of the grains to create bigger grains is possible only within the spheres. The process of crystallization may result in inhomogeneous distribution of RI inside the sphere. The aspects of inhomogeneous RI distribution are discussed in Sec. IV B.

## B. Perturbation due to inhomogeneous internal RI distribution

Annealing of the amorphous spheres resulted in polycrystalline spheres (PCSs). The grains of the polycrystalline sphere being anisotropic can perturb the local RI. The grain size distribution can modify the RI distribution throughout the sphere. Annealing of an isolated sphere can lead to a radial distribution of RI. To understand the effect of this internal inhomogeneity in RI, we have chosen two of the simplest possible models: (1) a sphere tessellated with Voronoi cells representing grains and (2) a sphere with the core-shell RI structure. The first model is discussed using discrete dipole approximation and second is discussed with the Aden-Kerker theory in Subsections IV B 1 and IV B 2. The perturbation due to the internal morphology could be more complicated. Some of the possible practical contributions are discussed in Subsection IV B 3.

### *1. Study of MDR modes of a polycrystalline sphere with birefringent grains using discrete dipole approximation (DDA)*

DDA calculations of the scattering spectrum are performed for a birefringent polycrystalline sphere to demonstrate the effect of large grains in a polycrystalline sphere. In DDA, the polarizable medium is modeled in terms of periodically arranged polarizable entities (dipoles) with a spacing $d$ such that $d < 1/(nk)$. Appendix B presents a brief description of the DDA method.[41,42] In the present context, a sphere of diameter 600 nm is constructed by arranging the dipoles on a cubical lattice. As the DDA calculations are computationally intensive, particularly when the resonant modes are to be studied, the required number of dipoles were ascertained as

follows: the scattering spectrum is first calculated by assigning an isotropic polarizable tensor to each entity, obtained from the weighted average of ordinary and extraordinary refractive index, $n = (2n_o + n_e)/3$, to each of the dipoles. The scattering spectrum calculated with about $10^6$ number of dipoles showed MDR modes with no distortion or splitting. Using this number of dipoles, polycrystalline spheres with 100 (PCS100), 1000 (PCS1000), and 10 000 (PCS10000) number of grains are constructed by grouping the dipoles into 100, 1000, and 10 000 Voronoi cells, respectively, using Neper software (version 3.2.0).[43] Voronoi cells representing grains are assigned polarizability tensors generated by performing rotational transformations, randomly in 3-dimension, on the diagonal polarizability tensor, with $\alpha_{xx} = \alpha_{yy} = \alpha_o$ (ordinary polarizability) and $\alpha_{zz} = \alpha_e$ (extraordinary polarizability) to model a polycrystalline sphere. The resulting polycrystalline sphere (PCS) made of tessellated Voronoi cells is shown schematically in Fig. 11.

Each colored region in Fig. 11 indicates a grain with a particular orientation of refractive index ellipsoid with respect to the lab frame. $Q_{sca}$, calculated for the PCS and EIS, are compared over a spectral range chosen such that the imaginary part of the RI and hence absorption coefficient is negligible. For these calculations, the direction of propagation and polarization of the incident electric field is taken along $x$- and $y$-axes, respectively.

The effects of grain size on the MDR modes are demonstrated in Fig. 12(a). The corresponding distributions of sizes of the grains can be observed in Fig. 12(b). The distribution of the grains is kept lognormal in nature to resemble the distribution of polycrystalline grains observed. When the number of grains is increased, the width of the distribution gets narrower and the mean value of the distribution decreases.

The scattering spectrum of the PCS resembles that of the EIS, except in the regions near the modes for all the three cases.

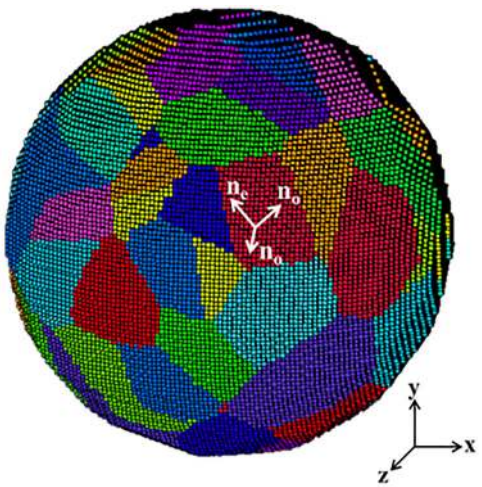


**FIG. 11.** Schematic of polycrystalline sphere indicating Voronoi cells as colored regions. The local coordinate system associated with a cell is shown rotated randomly with respect to the global coordinate system shown at the bottom right. Cells are tessellated such that there are no gaps between them.

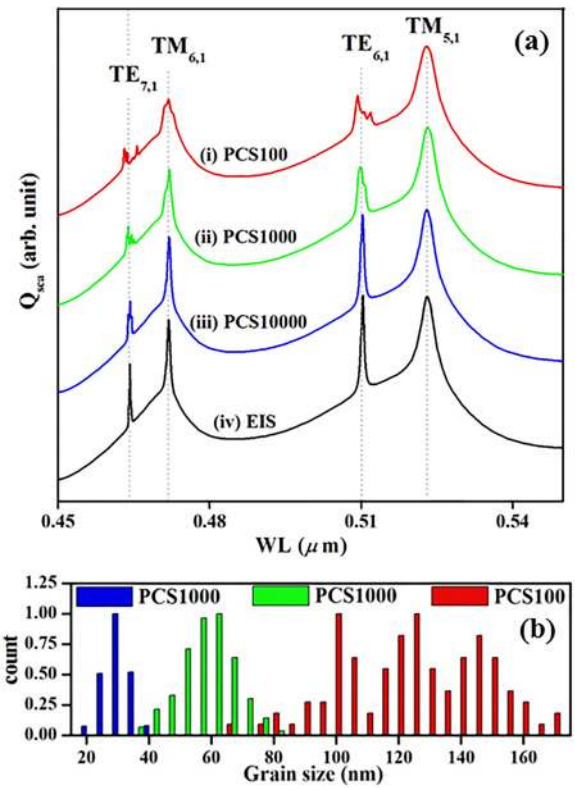


**FIG. 12.** (a) Scattering efficiency spectrum of the polycrystalline sphere (diameter = 600 nm) with (i) 100 (PCS100), (ii) 1000 (PCS1000), (iii) 10 000 (PCS10000) number of grains, and (iv) for the equivalent isotropic sphere (EIS) are shown. (b) Normalized distribution of grain sizes with number of grains equal to 100 (PCS100), 1000 (PCS1000), and 10 000 (PCS10000) are shown in red, green, and blue colors, respectively.

The difference is higher for the modes with higher values of $l$. The $TM_{5,1}$ mode is observed to retain its Lorentzian shape in all three polycrystalline sphere cases. However, the peak corresponding to $TM_{6,1}$ shows deviation from its Lorentzian shape in both PCS100 and PCS1000, although it is not split. $TM_{6,1}$ is perfectly Lorentzian in PCS10000 resembling that of EIS. Splitting can be observed in the $TE_{6,1}$ mode in PCS100. In the case of PCS1000, a deformed Lorentzian can be observed at the position corresponding to $TE_{6,1}$ without splitting. The $TE_{6,1}$ mode in PCS10000 is Lorentzian in nature. $TE_{7,1}$ shows splitting in all the polycrystalline spheres.

All the split modes are observed to be spread around the mode positions of the EIS. This spread is minimum in PCS10000 and maximum in PCS100. Simulations clearly indicate that (i) a large number of small grains reduces the effect of perturbation and modes approach the shapes and positions of that of the EIS, (ii) modes with lower value of $l$ are least affected by perturbation and resemble that of EIS, and (iii) the effect of perturbation is increasingly seen on modes with larger $l$. These trends are also shown by experimental MDR modes (see Table I) confirming the role of polycrystallinity in influencing the MDR mode structure.

In the case of randomly distributed grains, maximum and minimum ERI of a particular grain lies in the range set by $n_e$ and $n_o$ depending on its orientation with respect to the electric field. This implies that $\delta\varepsilon_r$ can have both positive and negative values when referenced to the weighted average value. When grains are equally oriented in all directions, both positive and negative shifts of the modes are equally possible, resulting in broadened and split modes with respect to that of EIS as is indeed observed in the calculated spectra.

### 2. Study of MDR modes of a layered sphere with a core-shell structure

While the splitting of the MDR modes and their dependence on $l$ and $\rho$ can be demonstrated, through DDA calculations, by considering larger grains to perturb the modes (see Table I), the relative shifts observed in the experimental spectrum (see Fig. 9) of the mode positions for $\rho = 1$ mode with respect to that for $\rho = 2$ modes appear to go beyond this model. The relative shift is negligible in S-500 but prominent in S-700, as can be clearly observed in Figs. 3 and 4 as well as from Tables II and III. Furthermore, it can be observed from Figs. 3 and 4 that, for the present consideration (size, RI, and WL range), $TE_{l,1}$ occurs between $TE_{l',2}$ and $TM_{l-1,1}$. The relative shift in $TE_{l,1}$ as compared to neighboring $TE_{l',2}$ and $TM_{l-1,1}$ observed in the experimental spectrum is quite unlike what randomly oriented crystalline grains would produce as discussed in Sec. IV B 1.

A possible reason behind these trends may be the inhomogeneous growth mechanism of the crystal grains on annealing. Rahman *et al.*[32] have shown that annealing of amorphous $TiO_2$ at a high temperature may result in inhomogeneous growth of the crystals. As discussed in Sec. III B, the synthesized spheres have a random grain size distribution and are a little porous. During annealing, the heat flow is radially inward from the outer surface and could lead to larger crystal grains near the surface compared to those in the interior core region. Porosity would also reduce as well due to increased grain sizes in the radially inward direction. These changes in the radial distributions in grain sizes and in porosity would lead to the radial variation of RI. Taking these considerations into account, it is surmised that the radial variation in RI is such that the outer layer would have a higher RI (due to larger grains and reduced porosity) as compared to that of the inner layer resulting in a core-shell type structure. Annealing at the two different temperatures would result in two different radial distributions in RI. It is indeed shown below that, using the scattering theory developed by Aden and Kerker[44] (Appendix C), the observed trend of the MDR spectrum could result from a core-shell type perturbation in RI.

Implementation of the Aden-Kerker theory requires the RIs of the core and shell along with the core radius and shell thickness to be known. If the radius of the microsphere is obtained from measurements, there would be three unknowns. We recall that, for an isotropic and homogenous sphere, (a) the RI extracted using $\rho = 2$ modes would have little difference from the RI extracted using $\rho = 1$ modes,[16] (b) the RI extracted from the spectral positions of TE modes should agree with that of TM modes as well, and (c) the internal field maxima for $\rho = 2$ modes occur further inward from the surface than those for $\rho = 1$ modes. Anticipating that a layered medium, with a core RI distinct from the shell RI, would not show all these trends, we proceed as follows: In the first step, a value of 2.3 is taken for the core RI that is close to but lower than the average extracted ERI (2.307) obtained from the experimental spectral positions using the $\rho = 2$ modes and the measured diameter of the sphere. The diameter of the sphere is chosen to be comparable to that of the experimentally measured value. A value of RI = 2.4 is chosen for the shell keeping in mind that the shell's RI is not expected to be too different from the core and ensuring that all the mode characteristics of interest are captured.

The mode positions of a layered sphere with core RI = 2.3 and shell RI = 2.4 are calculated over the entire range of shell thickness

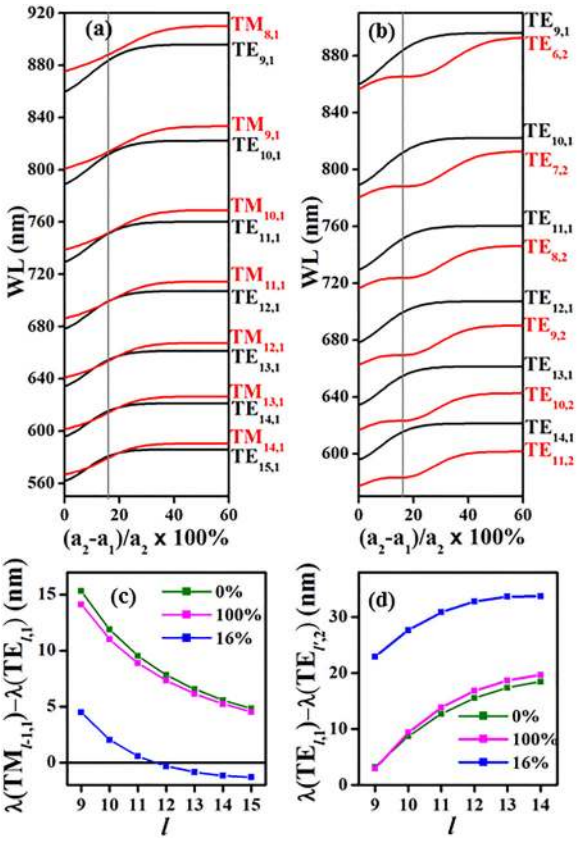


**FIG. 13.** Loci of the spectral position vs ratio of shell thickness to shell radius, in percentage, is plotted for (a) $TE_{l,1}$ (black) and $TM_{l,1}$ (red) and (b) $TE_{l,1}$ (black) $TE_{l',2}$ (red) for different values of $l$. For 16% shell thickness [gray line in (a) and (b)], the separations of the $TE_{l,1}$ mode to its neighboring $TM_{l-1,1}$ and $TE_{l',2}$ modes are shown (blue) in (c) and (d), respectively, as a function of $l$. The mode separations for 0% (green) and 100% (magenta) shell thickness are also included for comparison. The experimental trends in separations as a function of $l$ are found to correspond closely to the trends noted for 16% shell thickness.

by varying core-shell ratio for a sphere of diameter 1.5 $\mu$m. The spectral positions as a function of the ratio of shell thickness to shell radius (in percentage) are compared for (a) $TE_{l,1}$ (black) and $TM_{l-1,1}$ (red) and (b) $TE_{l,1}$ (black) and $TE_{l',2}$ (red) for different values of $l$ in Figs. 13(a) and 13(b), respectively.

Shell thicknesses corresponding to 0% and 100% ratio indicate isotropic spheres of radius 1.5 $\mu$m with an RI equal to that of only core (2.3) and only shell (2.4), respectively. Peak positions obtained from the core-shell model are compared with those corresponding to homogeneous spheres with shell thicknesses 0% and 100%. Modes computed for the sphere with a higher RI (2.4) get red shifted when compared to that evaluated with a lower RI (2.3). Moreover, mode positions of the layered sphere lies between that of the two homogeneous spheres with an RI of only the core and that of only the shell. Mode positions of the layered structure are dependent on the thickness of the shell and are different for modes with different polarizations (TE/TM), $l$ and $\rho$. It can be observed that when the shell thickness is high (>50%), there is a little shift on further increasing the thickness, and the mode positions remain same as that of the homogeneous sphere with an RI of 2.4 (100% shell). When the thickness is small, all modes get red shifted from the positions corresponding to the homogeneous sphere with an RI of 2.3 (0% shell). However, the trend of this shift is different for modes with different polarization and $\rho$. It can be observed in Fig. 13(a) that the $TE_{l,1}$ first approaches its neighboring $TM_{l-1,1}$ and then moves away as the shell thickness increases. Moreover, the separation between $TE_{l,1}$ and $TM_{l-1,1}$ reduces as $l$ increases. For $l > 11$, this separation is observed to be negative for a certain range of thickness (for example, for $TM_{11,1}$ and $TE_{12,1}$ in the range 13%–18%).

To capture the observed trends of separation of mode positions of $TM_{l-1,1}$ to that of $TE_{l,1}$ in this range, we choose a shell thickness of 16% [as indicated by the vertical gray line in Fig. 13(a)] and proceed for further analysis. The separation of mode positions of $TM_{l-1,1}$ to that of $TE_{l,1}$ as a function of $l$ is presented in Fig. 13(c). It can be observed in Fig. 13(c) that as $l$ increases, the separation between $TE_{l,1}$ and $TM_{l-1,1}$ decreases, changes sign, and approaches a constant. When the separation is too small to be distinguished, neighboring $TE_{l,1}$ and $TM_{l-1,1}$ modes appear merged. Such trends are indeed observed in the experimental spectrum of S-700 (see Fig. 4). In the MDR spectrum of S-700, it is difficult to distinguish the neighboring $TE_{l,1}$ and $TM_{l-1,1}$ mode from each other when $l > 11$. In the case of the two-layered sphere, for larger $l$, $TE_{l,1}$ and $TM_{l-1,1}$ appear very close to each other, changing the sequence of their appearance. A decrease in the RI of the shell below 2.4 would show either merging at higher $l$ or no merging effect at all, but would result in the reduction of the separation between neighboring $TE_{l,1}$ and $TM_{l-1,1}$ modes. Furthermore, the separation between $TE_{l,1}$ and its neighboring $TE_{l',2}$ seems to increase first and then reduce to a constant value as the thickness increases as shown in Fig 13(b). For a particular thickness of the shell, this separation increases to a constant value with increasing $l$ as shown in Fig. 13(d).

When the RI of the shell is taken to be lower than that of the core, the spectral separation between neighboring $TE_{l,1}$ and

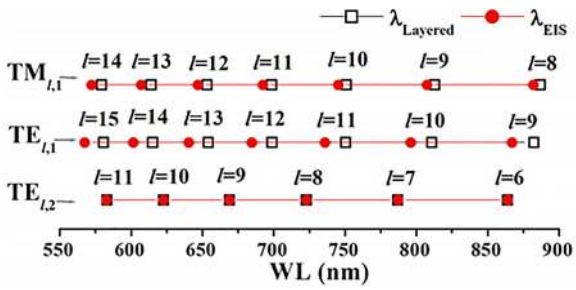


**FIG. 14.** Mode positions of the layered sphere with a 16% thick shell along with that of the EIS represented by open squares and filled red circles respectively.

$TM_{l-1,1}$ modes are observed to increase and that between $TE_{l,1}$ and $TE_{l',2}$ are observed to decrease with the shell thickness—trends just opposite to what is observed experimentally.

Treating the layered sphere of 1.5 $\mu$m diameter to be equivalently isotropic, an ERI of 2.324 was extracted using the $\rho = 2$ modes using the same method followed earlier for the experimental spectrum. When the MDR spectrum computed with the ERI = 2.324 was compared with that of the layered sphere, the $\rho = 1$ modes in the layered sphere are observed to be red shifted as shown in Fig. 14. The observed red shifts are more in TE modes than in TM modes for $\rho = 1$. Such shifts are not observed in TE modes with $\rho = 2$. These trends in shifts correspond closely to that observed in experimental modes of S-700 (see Fig. 9).

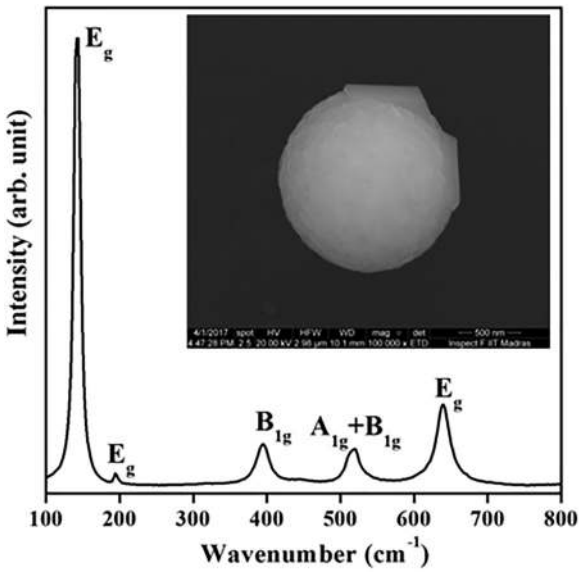


**FIG. 15.** Raman spectrum and (inset) SEM image of the sphere annealed at 900 °C.

### 3. MDR modes of spheres with complex internal morphology

Models discussed in Subsections IV B 1 and IV B 2 are the simplest possible models. However, the actual internal morphology of the spheres could be more complicated. There is a possibility of growth of few bigger grains in the interior of the sphere close to the surface though the surface remains smooth enough from the outside.

When spheres were annealed at a higher temperature (900 °C) for the same time period (2 h), growth of single crystalline grains was clearly visible in its SEM image as shown in the inset of Fig. 15. Raman spectrum of the spheres shown in Fig. 15 indicates its phase to be anatase. PL spectra collected for these spheres had features that were not characterizable.

Spheres corresponding to S-500 and S-700 may also have grains much bigger than the average grain size in the interior of the structure though the outer surface remained smooth. Annealing below 700 °C may not result in grains big enough to distort all the modes in the entire range of interest but does affect the modes with a higher value of $l$. In the presence of such bigger grains, the shift and split in the MDR modes are dependent on the position as well as the orientation of these bigger grains.

## V. DISCUSSION

Titanium dioxide is a birefringent material in its all three forms. Refractive indices and birefringence of $TiO_2$ are high compared to most of the other dielectric materials with optical applications. $TiO_2$ has been suggested as MDR resonators for its unique optical and material properties. Most of the chemical synthesis methods of $TiO_2$ result in the amorphous phase. Heat treatments like annealing can result in crystallization of the spheres. Crystalline forms of $TiO_2$ with large grain sizes are more stable with respect to phase change. However, birefringent grains of bigger sizes can introduce perturbation in the MDR modes. Furthermore, annealing at a higher temperature may lead to inhomogeneous crystallization leading to inhomogeneous radial RI distribution. Perturbation due to such synthesis techniques can result in shifting and/or splitting of the MDR modes.

For a polycrystalline sphere to behave like an affective homogeneous isotropic medium, the grains must be quite small when compared with the wavelength, grain size distribution should be fairly narrow, and there should be no preferred orientation of their crystal axis. DDA simulations show that when the orientations of the grains are random and orientation angles are equally distributed, modes continue to lie close to the corresponding modes of EIS but with split modes occurring around the corresponding modes of EIS. The effect of perturbation is observed more in modes with a large $l$ and a small $\rho$.

Radially inhomogeneous growth of grains due to annealing at higher temperatures is surmised to result in a core-shell layering. For the core of the layered sphere that is concentric with the shell, degeneracy with respect to $m$ is not lifted, but the modes show relative shifts when compared to their EIS. Relative spacing of the neighboring modes with different polarization (TE/TM) and $\rho$ become different from that of an isotropic sphere with the same ERI. However, it is shown in the present work that identification of modes with higher $\rho$ and lower $l$ is still possible with the proposed mode identification method.[16]

The actual internal morphology of the sphere may be further complicated with the presence of birefringent grains much bigger than the average RI of the sample. In that case, shifting and splitting of the modes are dependent on the position and orientation of the grain in the interior of the sphere.

## VI. SUMMARY AND CONCLUSIONS

MDR modes are observed in the PL spectrum of polycrystalline anatase $TiO_2$ microspheres. A method of preparation was chosen to provide a good starting amorphous material. Annealing procedures were adopted to control the grain sizes suitably. After the preparation, near-perfect spheres annealed at T = 500 °C and T = 700 °C were chosen for systematic investigations of the MDR modes. Instances where crystals explicitly projected beyond the surface could be seen when annealing was done at a higher temperature (900 °C). As near-perfect spheres were chosen for this study, effects other than polycrystallinity, such as slight porosity, nonsphericity, and roughness of the surface, were also investigated. The MDR modes of spheres annealed at a higher temperature show splits and shifts with respect to that of the simulated MDR modes of EIS obtained from the extracted RI. Effects of perturbation observed in the MDR modes are discussed in terms of shape deviations from a perfect sphere as well as that of inhomogeneous RI distribution. The effect of perturbation due to nonsphericity is very less in S-700 than that in S-500. However, effects of inhomogeneity in RI enhance the perturbation in the MDR modes of S-700 as compared to S-500. Splitting and deformation of modes with higher values of $l$ are demonstrated to arise from a polycrystalline sphere consisting of larger grains when computed using DDA. The existence of relative shifts of the $\rho = 1$ modes is demonstrated in terms of a core-shell structure for the RI through computations based on the Aden-Kerker theory. The possibility of a further complicated internal morphology is also discussed.

The investigations carried out suggest that the nature of inhomogeneity of the RI within the microsphere can be ascertained from the observed spectral features with the aid of computations. The present work extends the scope of model-assisted investigations in understanding morphology dependent resonators and indicates the possibility of designing resonators with prescribed refractive index features. In particular, there appears a possibility for obtaining the desired mode characteristics from stable polycrystalline anatase phase $TiO_2$ resonators through control of the heat treatment.

## ACKNOWLEDGMENTS

We acknowledge the HPCE, IIT Madras, for the high performance computing facility.

## APPENDIX A: SPECTRAL POSITIONS OF EXPERIMENTAL MDR MODES AND THAT OF THE CORRESPONDING EIS

**TABLE II.** Spectral mode positions corresponding to experiment and EIS for S-500.

| | $TE_{l,1}$ | | $TM_{l,1}$ | | $TE_{l,2}$ | |
|---|---|---|---|---|---|---|
| L | $\lambda_{l,1}^{exp}$ (nm) | $\lambda_{l,1}^{EIS}$ (nm) | $\lambda_{l,1}^{exp}$ (nm) | $\lambda_{l,1}^{EIS}$ (nm) | $\lambda_{l,2}^{exp}$ (nm) | $\lambda_{l,2}^{EIS}$ (nm) |
| 7 | … | … | … | … | 720.95 | 719.75 |
| 8 | … | … | 856.85 | 854.82 | 708.01 | 708.35 |
| 9 | 839.65 | 839.28 | 787.76 | 785.9 | 659.46 | 659.73 |
| 10 | 775.34 | 774.15 | 730.43 | 728.92 | 618.34 | 618.53 |
| 11 | 720.95 | 719.75 | 681.88 | 680.98 | 583.19 | 583.34 |
| 12 | 674.76 | 673.64 | 640.8 | 640.07 | 552.99 | 553.01 |
| 13 | 634.63 | 634.08 | 605.48 | 604.88 | | |
| 14 | 600.08 | 599.83 | 574.54 | 573.87 | | |
| 15 | 569.89 | 569.8 | 547.44 | 547.06 | | |
| 16 | 543.51 | 543.44 | | | | |

**TABLE III.** Spectral mode positions corresponding to experiment and EIS for S-700.

| | $TE_{l,1}$ | | $TM_{l,1}$ | | $TE_{l,2}$ | |
|---|---|---|---|---|---|---|
| l | $\lambda_{l,1}^{exp}$ (nm) | $\lambda_{l,1}^{EIS}$ (nm) | $\lambda_{l,1}^{exp}$ (nm) | $\lambda_{l,1}^{EIS}$ (nm) | $\lambda_{l,2}^{exp}$ (nm) | $\lambda_{l,2}^{EIS}$ (nm) |
| 7 | … | … | … | … | 738.14 | 738.35 |
| 8 | … | … | 824.36 | 822.21 | 683.23 | 683.48 |
| 9 | 812.27 | 807.79 | 758.58 | 756.82 | 637.67 | 637.4 |
| 10 | 750.15 | 745.96 | 704.8 | 702.83 | 599.29 | 598.48 |
| 11 | 697.77 | 694.38 | | | 564.72 | 565.32 |

## APPENDIX B: DISCRETE DIPOLE APPROXIMATION

The discrete dipole approximation (DDA),[41,42] considers the medium to be made of discrete polarizable entities spaced periodically with the period $d$ such that $|n|kd < 1$. Each entity at the $i$th position is assigned a polarizability tensor $\boldsymbol{\alpha}_i$. The dipole moment at each position is calculated solving Eq. (B1) iteratively,

$$\mathbf{p}_i = \boldsymbol{\alpha}_i \left( \mathbf{E}_{inc,i} - \sum_{j \neq i} \mathbf{A}_{ij} \mathbf{p}_j \right), \tag{B1}$$

where $\mathbf{E}_{inc,i}$ is the incident electric field at the $i$th position and $-\mathbf{A}_{ij}\mathbf{p}_j$ is the electric field at the $i$th position due to the dipole at the $j$th position as given in Eqs. (B2) and (B3),

$$\mathbf{A}_{ii} = \alpha_i^{-1}, \quad i = j, \tag{B2}$$

$$\mathbf{A}_{ij}\mathbf{p}_j = \frac{\exp(ikr_{ij})}{r_{ij}^3} \left[ k^2 \mathbf{r}_{ij} \times (\mathbf{r}_{ij} \times \mathbf{p}_j) + \frac{(1 - ikr_{ij})}{r_{ij}^2} \times \{ r_{ij}^2 \mathbf{p}_j - 3\mathbf{r}_{ij}(\mathbf{r}_{ij} \cdot \mathbf{p}_j) \} \right], \quad i \neq j. \tag{B3}$$

Extinction, absorption, and scattering cross section can be calculated from the dipole moment of each dipole as give in Eqs. (B4), (B5), and (B6), respectively.

$$C_{ext} = \frac{4\pi k}{|E_{inc}|^2} \sum_{i=1}^{N} \mathrm{Im}(\mathbf{E}_{inc,i}^{*} \cdot \mathbf{p}_i), \tag{B4}$$

$$C_{abs} = \frac{4\pi k}{|E_{inc}|^2} \sum_{i=1}^{N} \left\{ \mathrm{Im}[\mathbf{p}_i \cdot (\alpha_i^{-1})^{*} \mathbf{p}_i^{*}] - \frac{2}{3} k^3 |\mathbf{p}_i|^2 \right\}, \tag{B5}$$

$$C_{sca} = C_{ext} - C_{abs}. \tag{B6}$$

## APPENDIX C: MDR MODES IN A TWO-LAYERED SPHERE

According to the Aden and Kerker theory,[9,44] the scattering efficiency cross section of a layered sphere with radius and RI for core $a_1$ and $n_1$ and that for the shell $a_2$ and $n_2$ is given by

$$Q_{sca} = \frac{2\pi}{|k|^2} \sum_{n=1}^{\infty} (2l + 1)(|a_l|^2 + |b_l|^2). \tag{C1}$$

$a_l$ and $b_l$ in Eq. (C1) are the scattering coefficients given in Eqs. (C2) and (C3), respectively,

$$a_l = \frac{\psi_l(x_2)[\psi'_l(n_2x_2) - A_l\chi'_l(n_2x_2)] - n_2\psi'_l(x_2)[\psi_n(n_2x_2) - A_l\chi_l(n_2x_2)]}{\xi_l(x_2)[\psi'_l(n_2x_2) - A_l\chi'_l(n_2x_2)] - n_2\xi'_l(x_2)[\psi_n(n_2x_2) - A_l\chi_l(n_2x_2)]}, \tag{C2}$$

$$b_l = \frac{n_2\psi_l(x_2)[\psi'_l(n_2x_2) - B_l\chi'_l(n_2x_2)] - \psi'_l(x_2)[\psi_l(n_2x_2) - B_l\chi_l(n_2x_2)]}{n_2\xi_l(x_2)[\psi'_l(n_2x_2) - B_l\chi'_l(n_2x_2)] - \xi'_l(x_2)[\psi_l(n_2x_2) - B_l\chi_l(n_2x_2)]}, \tag{C3}$$

where $x_2 = ka_2$ and $\psi$, $\chi$, and $\xi$ are Riccati-Bessel functions defined in Eqs. (C4), (C5), and (C6), respectively,

$$\psi_l(z) = zj_l(z), \tag{C4}$$

$$\chi_l(z) = -zy_l(z), \tag{C5}$$

$$\xi_l(z) = zh_l^{(1)}(z), \tag{C6}$$

with $j_l$, $y_l$, and $h_l^{(1)}$ being the spherical Bessel, spherical Neumann, and spherical Hankel functions of the first kind, respectively. $A_l$ and $B_l$ in Eqs. (C2) and (C3) are defined as

$$A_l = \frac{n_2\psi_l(n_2x_1)\psi'_l(n_1x_1) - n_1\psi'_l(n_2x_1)\psi_l(n_1x_1)}{n_2\chi_l(n_2x_1)\psi'_l(n_1x_1) - n_1\chi'_l(n_2x_1)\psi_l(n_1x_1)}, \tag{C7}$$

$$B_l = \frac{n_2\psi'_l(n_2x_1)\psi_l(n_1x_1) - n_1\psi_l(n_2x_1)\psi'_l(n_1x_1)}{m_2\chi'_l(n_2x_1)\psi_l(n_1x_1) - n_1\chi_l(n_2x_1)\psi'_l(n_1x_1)}, \tag{C8}$$

where $x_1 = ka_1$. An MDR mode corresponding to TM and TE occurs in a layered sphere when the denominator of $a_l$ and $b_l$ vanishes respectively. The resonance condition can be stated as[44]

$$A_l(n_1, n_2, x_1) = \alpha_l(n_2, x_2) \quad \text{for the TM mode} \tag{C9}$$

and

$$B_l(n_1, n_2, x_1) = \beta_l(n_2, x_2) \quad \text{for the TE mode,} \tag{C10}$$

such that

$$\alpha_l = \frac{\chi_l(x_2)\psi'_l(n_2x_2) - n_2\chi'_l(x_2)\psi_l(n_2x_2)}{\chi_l(x_2)\chi'_l(n_2x_2) - n_2\chi'_l(x_2)\chi_l(n_2x_2)}, \tag{C11}$$

$$\beta_l = \frac{\chi'_l(x_2)\psi_l(n_2x_2) - n_2\chi_l(x_2)\psi'_l(n_2x_2)}{\chi'_l(x_2)\chi_l(n_2x_2) - n_2\chi_l(x_2)\chi'_l(n_2x_2)}. \tag{C12}$$

Mode positions of a layered sphere can be obtained by solving Eqs. (C9) and (C10) for TM and TE modes, respectively.

## REFERENCES


[1]R. K. Chang and A. J. Campillo, *Optical Processes in Microcavities* (World Scientific Publishing Co. Pte. Ltd., London, 1996).

[2]J. M. Le Floch, J. D. Anstie, M. E. Tobar, J. G. Hartnett, P. Y. Bourgeois, and D. Cros, "Whispering modes in anisotropic and isotropic dielectric spherical resonators," Phys. Lett. A **359**, 1–7 (2006).

[3]J. Ward and O. Benson, "WGM microresonators: Sensing, lasing and fundamental optics with microspheres," Laser Photon. Rev. **5**, 553–570 (2011).

[4]M. R. Foreman, J. D. Swaim, and F. Vollmer, "Whispering gallery mode sensors," Adv. Opt. Photonics **7**, 168–240 (2015).

[5]G. Lin, A. Coillet, and Y. K. Chembo, "Nonlinear photonics with high-Q whispering-gallery-mode resonators," Adv. Opt. Photonics **9**, 828–888 (2018).

[6]P. Zijlstra, K. L. van der Molen, and A. P. Mosk, "Spatial refractive index sensor using whispering gallery modes in an optically trapped microsphere," Appl. Phys. Lett. **90**, 161101 (2007).

[7]H. E. Benner, P. W. Barber, J. F. Owen, and B. K. Chang, "Observation of structure resonances in the fluorescence spectra from microspheres," Phys. Rev. Lett. **44**, 475–478 (1980).

[8]S. Pang, R. E. Beckham, and K. E. Meissner, "Quantum dot-embedded microspheres for remote refractive index sensing," Appl. Phys. Lett. **92**, 221108 (2008).

[9]A. V. Veluthandath and P. B. Bisht, "Radiative rate modification in CdSe quantum dot-coated microcavity," J. Appl. Phys. **118**, 233102 (2015).

[10]C. Czekalla, T. Nobis, A. Rahm, B. Cao, J. Zúñiga-Pérez, C. Sturm, R. Schmidt-Grund, M. Lorenz, and M. Grundmann, "Whispering gallery modes in zinc oxide micro- and nanowires," Phys. Status Solidi B **247**, 1282–1293 (2010).

[11]R. Khanum, R. S. Moirangthem, and N. M. Das, "Observation of defect-assisted enhanced visible whispering gallery modes in ytterbium-doped ZnO microsphere," J. Appl. Phys. **121**, 213101 (2017).

[12]A. Paunoiu, R. S. Moirangthem, and A. Erbe, "Whispering gallery modes in intrinsic $TiO_2$ microspheres coupling to the defect-related photoluminescence after visible excitation," Phys. Status Solidi Rapid Res. Lett. **9**, 241–244 (2015).

[13]J. Park, S. K. Ozdemir, F. Monifi, T. Chadha, S. H. Huang, P. Biswas, and L. Yang, "Whispering gallery modes: Titanium dioxide whispering gallery microcavities," Adv. Opt. Mater. **2**, 711–717 (2014).

[14]M. C. Tsai, T. L. Tsai, D. B. Shieh, H. T. Chiu, and C. Y. Lee, "Detecting HER2 on cancer cells by $TiO_2$ spheres Mie scattering," Anal. Chem. **81**, 7590–7596 (2009).

[15]J. Zhang, X. Jin, P. I. M. Guzman, X. Yu, H. Liu, H. Zhang, L. Razzari, and J. P. Claverie, "Engineering the absorption and field enhancement properties of Au–$TiO_2$ nanohybrids *via* whispering gallery mode resonances for photocatalytic water splitting," ACS Nano **10**, 4496–4503 (2016).

[16]I. Kalyan and C. V. Krishnamurthy, "Morphology dependent resonance modes in highly porous $TiO_2$ microspheres," J. Appl. Phys. **124**, 133102 (2018).

[17]C. Baker, S. Stapfner, D. Parrain, S. Ducci, G. Leo, E. M. Weig, and I. Favero, "Optical instability and self-pulsing in silicon nitride whispering gallery resonators," Opt. Express **20**, 29076–29089 (2012).

[18]C. Tessarek, R. Röder, T. Michalsky, S. Geburt, H. Franke, R. S. Grund, M. Heilmann, B. Hoffmann, C. Ronning, M. Grundmann, and S. Christiansen, "Improving the optical properties of self-catalyzed GaN microrods toward whispering gallery mode lasing," ACS Photonics **1**, 990–997 (2014).

[19]G. E. Jellison, Jr., L. A. Boatner, J. D. Budai, B. S. Jeong, and D. P. Norton, "Spectroscopic ellipsometry of thin film and bulk anatase ($TiO_2$)," J. Appl. Phys. **93**, 9537–9541 (2003).

[20]T. K. Das, P. Ilaiyaraja, and C. Sudakar, "Whispering-gallery mode assisted enhancement in the power conversion efficiency of DSSC and QDSSC devices using $TiO_2$ microsphere photoanodes," ACS Appl. Energy Mater. **1**, 765–774 (2018).

[21]F. Carn, A. Colin, M.-F. Achard, H. Deleuze, C. Sanchez, and R. Backov, "Anatase and rutile $TiO_2$ macrocellular foams: Air-liquid foaming sol-gel process towards controlling cell sizes, morphologies, and topologies," Adv. Mater. **17**, 62–66 (2005).

[22]M. C. Mathpal, A. K. Tripathi, M. K. Singh, S. P. Gairola, S. N. Pandey, and A. Agarwal, "Effect of annealing temperature on Raman spectra of $TiO_2$ nanoparticles," Chem. Phys. Lett. **555**, 182–186 (2013).

[23]C. Jin, B. Liu, Z. Lei, and J. Sun, "Structure and photoluminescence of the $TiO_2$ films grown by atomic layer deposition using tetrakis-dimethylamino titanium and ozone," Nanoscale Res. Lett. **10**, 95 (2015).

[24]J. Lee, S. J. Lee, W. B. Han, H. Jeon, J. Park, H. Kim, C. S. Yoon, and H. Jeon, "Effect of crystal structure and grain size on photo-catalytic activities of remote-plasma atomic layer deposited titanium oxide thin film," ECS J. Solid State Sci. Technol. **1**, Q63–Q69 (2012).
[25]P. J. Martin and A. Bendavid, "Review of the filtered vacuum arc process and materials deposition," Thin Solid Films **394**, 1–14 (2001).
[26]A. N. Luiten, M. E. Tobar, J. Krupka, R. Woode, E. N. Ivanov, and A. G. Mann, "Microwave properties of a rutile resonator between 2 and 10 K," J. Phys. D Appl. Phys. **31**, 1383–1391 (1998).
[27]H. Ikari, K. Okanishi, M. Tomita, and T. Ishidate, "Fluorescence MDR features of $Eu^{3+}$ doped sol–gel $TiO_2$ hydrate microspheres," Opt. Mater. **30**, 1323–1326 (2008).
[28]Y. Arai, T. Yano, and S. Shibata, "High refractive-index microspheres of optical cavity structure," Appl. Phys. Lett. **82**, 3173–3175 (2003).
[29]J. A. Benavides, C. P. Trudeau, L. F. Gerlein, and S. G. Cloutier, "Laser selective photoactivation of amorphous $TiO_2$ films to anatase and/or rutile crystalline phases," ACS Appl. Energy Mater. **1**, 3607–3613 (2018).
[30]N. R. Nand, M. Goryachev, J. M. Le Floch, D. L. Creedon, and M. E. Tobar, "Hyperparametric effects in a whispering-gallery mode rutile dielectric resonator at liquid helium temperatures," J. Appl. Phys. **116**, 134105 (2014).
[31]K. He, G. Zhao, and G. Han, "Template-free synthesis of $TiO_2$ microspheres with tunable particle size via a non-aqueous sol–gel process," CrystEngComm **16**, 7881–7884 (2014).
[32]M. M. Rahman, G. Yu, T. Soga, T. Jimbo, H. Ebisu, and M. Umeno, "Refractive index and degree of inhomogeneity of nanocrystalline $TiO_2$ thin films: Effects of substrate and annealing temperature," J. Appl. Phys. **88**, 4634–4641 (2000).
[33]S. J. Chen, Z. Feng, T. Chen, Y. Lian, X. Wang, and C. Li, "Photoluminescence characteristics of $TiO_2$ and their relationship to the photoassisted reaction of water/methanol mixture," J. Phys. Chem. C **111**, 693–699 (2007).
[34]C. F. Bohren and D. R. Huffman, *Absorption and Scattering of Light by Small Particles* (Wiley Interscience Publication, 1998).
[35]H. M. Lai, P. T. Leung, K. Young, P. W. Barber, and S. C. Hill, "Time-independent perturbation for leaking electromagnetic modes in open systems with application to resonances in microdroplets," Phys. Rev. A **41**(9), 5187–5198 (1990).
[36]N. Riesen, T. Reynolds, A. François, M. R. Henderson, and T. M. Monro, "Q-factor limits for far-field detection of whispering gallery modes in active microspheres," Opt. Express **23**, 28896–28904 (2015).
[37]P.-T. Leung, S.-W. Ng, K.-M. Pang, and K.-M. Lee, "Morphology-dependent resonances in dielectric spheres with many tiny inclusions," Opt. Lett. **27**, 1749–1751 (2002).
[38]M. Ornigotti and A. Aiello, "Theory of anisotropic whispering-gallery-mode resonators," Phys. Rev. A **84**, 013828 (2011).
[39]C. C. Lam, P. T. Leung, and K. Young, "Explicit asymptotic formulas for the positions, widths, and strengths of resonances in Mie scattering," J. Opt. Soc. Am. B **9**, 1585–1592 (1992).
[40]P. Laven, "Simulation of rainbows, coronas, and glories by use of Mie theory," Appl. Opt. **42**, 436–444 (2003).
[41]C. M. Purcell and C. R. Pennypacker, "Scattering and absorption of light by nonspherical dielectric grains," Astrophys. J. **186**, 705–714 (1973).
[42]P. J. Flatau and B. T. Draine, "Discrete-dipole approximation for scattering calculations," J. Opt. Soc. Am. **11**, 1491 (1994).
[43]R. Quey, P. R. Dawson, and F. Barbe, "Large-scale 3D random polycrystals for the finite element method: Generation, meshing and remeshing," Comput. Methods Appl. Mech. Eng. **200**, 1729 (2011).
[44]R. L. Hightower and C. B. Richardson, "Resonant Mie scattering from a layered sphere," Appl. Opt. **27**, 4850–4855 (1988).